Dynamics of Nonlinear Optical Losses in Silicon-Rich Nitride Nano-Waveguides

Dmitrii Belogolovskii, Yeshaiahu Fainman, and Nikola Alic*

Free carrier absorption (FCA) is established to be the cause of nonlinear losses in plasma-enhanced chemical vapor deposition (PECVD) silicon-rich nitride (SRN) waveguides. To validate this hypothesis, a photo-induced current is measured in SRN thin films with refractive indices varying between 2.5 and 3.15 when a C-band laser light is illuminating the SRN films at various powers, indicating the generation of free carriers. Furthermore, nonlinear loss dynamics is, for the first time, measured and characterized in detail in SRN waveguides by utilizing high peak power C-band complex shape optical pulses for estimation of free carrier generation (FCG) and free carrier recombination (FCR) lifetimes and their dynamics. Both FCG and FCR are found to decrease with an increase in the refractive index of SRN, and, specifically, the FCR lifetimes are found (92 ± 7) ns, (39 ± 3) ns, and (31 ± 2) ns for the SRN indices of 2.7, 3, and 3.15, respectively. Lastly, nonlinear losses in high refractive index SRN waveguides are demonstrated to be minimized and altogether avoided when the pulse duration reduced below the free carrier generation lifetime, thus providing a way of taking a full advantage of the large inherent SRN nonlinear properties.

1. Introduction

Silicon-rich nitride (SRN) on insulator is a promising integrated photonics platform for nonlinear optics due to its large optical nonlinear response, which increases with higher concentration of Si.[1] Specifically, the third order susceptibility χ_3 of SRN grown by plasma-enhanced chemical vapor deposition (PECVD) with a refractive index of 3.2 (at 1550 nm) is around 12.6×10^{-19} m^2 V^{-2}, which is about four times larger than that of crystalline silicon (c-Si).[1] A particularly remarkable property of SRN is the ability to change its linear and nonlinear optical properties in a wide range by changing Si content in SRN thin film deposition and post-processing parameters. Specifically, changing these parameters allows optimization of the refractive index, optical nonlinearities, optical losses (including nonlinear optical losses), and optical transparency window, and thereby maximizing the efficiency of the SRN nonlinear response such as, for example, wave mixing.[1–3] Another beneficial property of SRN is its larger refractive index, allowing the light to be confined tighter in a waveguide, which is crucial for nonlinear wave mixing as it reduces the waveguide's effective mode area, thus, improving the overlap between the mode and nonlinear media. Indeed, the aforementioned set of circumstances enables efficient nonlinear processes in SRN devices such as four-wave mixing (FWM),[1,2] supercontinuum generation,[4–6] DC Kerr effect,[7] nonlinear Kerr switching,[8] intermodal frequency generation,[9] second harmonic generation.[10] Another advantage of the SRN platform is a relatively large electric field breakdown of around 100 V μm^{-1},[7] much larger than that of c-Si, around 40 V μm^{-1}.[11] It increases the efficiency of the devices that require application of strong electric field, such as electric field induced second harmonic generator (EFISHG) or linearized Kerr effect electro-optic modulator. Such devices were demonstrated on the c-Si and Si_3N_4 platforms,[11–13] and they are yet to be demonstrated on the SRN platform. Additionally, the thermo-optic coefficient of SRN also increases for higher refractive indices,[14] which led to demonstrations of efficient thermo-optic SRN devices such as bi-stable optical switcher,[15] thermo-optic phase shifter,[16] and optical phased array,[17] to name a few.

On the other hand, the seemingly outstanding potential for nonlinear optics applications of SRN is quenched by the existence of nonlinear optical losses that have been observed and described in SRN in our prior work.[1] Indeed, nonlinear losses in SRN were reported in multiple instances, and it was suggested that these are due to the two-photon absorption (TPA) process.[18,19] However, there are several mechanisms that can be the cause of nonlinear losses in optical waveguides, including TPA (and multi-photon absorption in general),[18] free carrier absorption (FCA),[20] stimulated Brillouin scattering (SBS),[21,22] stimulated Raman scattering (SRS),[23] self-phase modulation (SPM),[24,25] cross-phase modulation (XPM),[26] FWM,[1,2] and others. In fact, the effects that can give rise to nonlinear losses are distinguishable by the particular way they affect light propagation in waveguides. For instance, all the mentioned processes have very

D. Belogolovskii, Y. Fainman, N. Alic
University of California
San Diego, 9500 Gilman Drive, La Jolla, CA 92093, USA
E-mail: dbelogol@ucsd.edu

The ORCID identification number(s) for the author(s) of this article can be found under https://doi.org/10.1002/adom.202401299

DOI: 10.1002/adom.202401299

different generation and relaxation dynamics, with TPA being characterized as ultra-fast, due to its dynamics being only limited by electron transition times, thus allowing it to be observed even when short femtosecond optical pulses are utilized.[27] Conversely, nonlinear processes such as SPM, XPM, and FWM induce a spectral change in a propagating optical signal, hence their contribution can be confirmed by changes in the optical spectrum of the transmitted or reflected light.[1,2,24–26] On the other hand, FCA can have very diverse dynamics depending on the material properties, waveguide geometry, and optical power, owing to the variety of different mechanisms of the free carrier generation and recombination processes. Specifically, Auger, Shockley–Read–Hall (nonradiative), radiative, surface recombination processes are responsible for free carrier absorption, while TPA and defects (with energy states in a bandgap serving as recombination-generation (R-G) centers) are responsible for free carrier generation,[20,28–30] affecting the FCA dynamics substantially. In addition, it is important to emphasize that FCA does not lead to any spectral change of a propagating optical signal at a given optical frequency/wavelength, making it impossible to be identified by a mere measurement of the signal transmission spectrum.[28] Therefore, it can be problematic, at best, to confirm that any observed nonlinear loss is caused by FCA. Nonetheless, there are different ways to identify this loss mechanism. For example, the latter can be accomplished by measuring the loss dependence on the wavelength of light and comparing it to the predictions of the Drude model,[31–33] which specifically predicts higher losses for longer wavelengths. Alternatively, FCA dynamics can be characterized to estimate the recombination lifetime to determine the presence of particular recombination mechanisms such as Auger, or Shockley–Read–Hall recombination.[29,34] In fact, FCA is commonly observed in c-Si and amorphous silicon (a-Si) waveguides in C-band. Here TPA generates free carriers, leading to nonlinear optical losses that limit applications of Si in nonlinear optics.[30,35–37] In addition, we previously observed nonlinear losses in SRN waveguides with refractive indices larger than 2.7 in C-band for the continuous wave (CW) operation.[1] However, we established that such losses are not caused by TPA as demonstrated by the observation of linear transmission of high peak power short optical pulses (5 W, 200 fs) at the repetition period of 100 ns.[1] Those results clearly established that the cause of the losses had a generation lifetime longer than 200 fs. We also determined that such losses cannot be due to SBS, SRS, SPM, XPM, FWM nonlinear processes mentioned above.[1]

In this manuscript, we conduct a comprehensive investigation into the cause of the nonlinear losses observed in PECVD SRN waveguides and present detailed results on their dynamics. Furthermore, we provide evidence that the observed nonlinear optical losses in our SRN waveguides are caused by FCA. Specifically, we measured electrical current in SRN thin films across a range of refractive indices from 2.5 to 3.2 to determine the presence of free carriers. During the measurements, C-band laser light was incident on the films while a DC electric field was applied. In this setup, indeed, we observed a photo-induced current (photocurrent), which was found to increase exponentially with the SRN waveguide refractive index, indicating the generation of free carriers under light illumination. This finding, to the best of our knowledge, is a novel result. In addition, we introduce a novel approach for measuring both generation and recombination dynamics of the nonlinear losses induced by FCA in SRN waveguides. This approach is based on a single complex shape optical signal pulse source, as opposed to the common pump-probe approach where both optical pump pulse and signal are used.[34] Notably, free carrier generation and recombination dynamics were characterized for various SRN waveguides across a range of refractive indices and optical powers, and the new finding reveals that as the SRN refractive index increases, both generation and recombination lifetimes decrease. Most importantly, it was demonstrated that nonlinear losses can be minimized or altogether avoided by utilizing optical pulses shorter than the generation lifetime, while ensuring that the repetition period of the pulses is longer than the recombination lifetime. Thus, this approach enables the exploitation of the large nonlinear properties of SRN while avoiding nonlinear losses. Here we also want to note that our PECVD SRN deposition recipe is unique to our group, therefore the obtained results may be different for various SRN preparation methods (such as low-pressure chemical vapor deposition (LPCVD), inductively coupled plasma chemical vapor deposition (ICPCVD), PECVD, etc.) and specific recipes used by other research groups.

The manuscript is organized as follows: The photocurrent experiment conducted in SRN thin films is analyzed and described in Section 2, characterization and analysis of the nonlinear loss dynamics observed in SRN waveguides is presented in Section 3, whereas the discussion of the findings and conclusions are summarized in Section 4.

2. Photo-Induced Current in SRN Thin Films

2.1. Fabrication and Setup

The primary purpose of this section is to demonstrate that the observed nonlinear optical losses in SRN waveguides in C-band are caused by FCA due to photo-induced free carriers generated in SRN. Indeed, in this case photocurrent ought to be observed in a high refractive index SRN thin film when C-band laser light is incident on the film, due to the generated free carriers. Furthermore, a proper approach should consist of measuring the photocurrent in SRN film samples with varying refractive indices in order to ensure that the photocurrent increases with the refractive index, similarly to the trend observed in the associated nonlinear optical losses in SRN waveguides. With that objective, five different SRN film samples with different indices (2.5, 2.65, 2.85, 2.95, and 3.15) were fabricated and characterized. In particular, **Figure** 1a,b demonstrate two different fabrication flows implemented for our SRN samples. Specifically, in the first approach described in Figure 1a, a Heidelberg MLA 150 photolithography equipment was used to expose an electrode pattern, followed by Au sputtering in a Denton 635 sputter system, after which the lift-off was implemented in a Remover PG. Finally, SRN thin film and SiO_2 cladding were deposited in an Oxford Plasmalab PECVD system on the top of the sample. Note that for SRN deposition, the pressure was 650 mTorr, chamber temperature was 350 °C, high frequency (HF) power was 20 W, the precursor gases were SiH_4 with N_2. The ratio of the gases was altered to control the refractive index of the deposited SRN film. For greater details, we refer to our previous work, where we plot a refractive index as a function of the gases ratio (Figure 1).[1] It is also worth

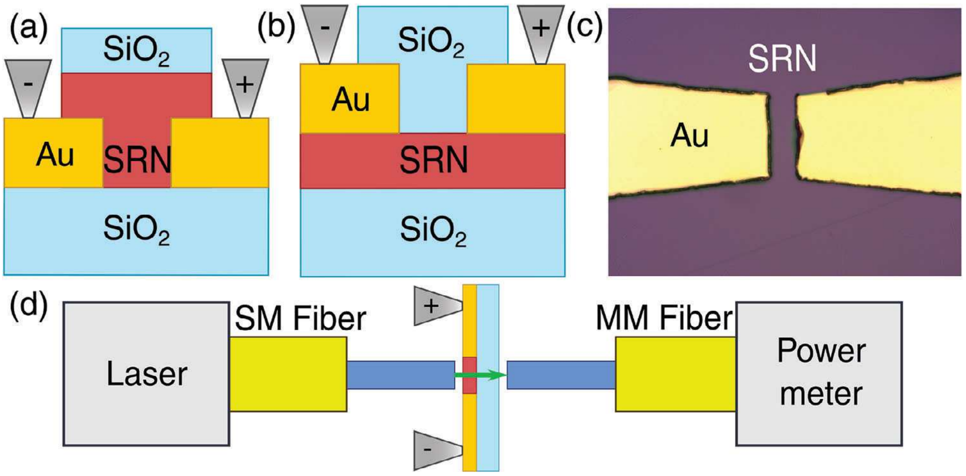

Figure 1. Schematic of a fabricated SRN sample with electrodes where a) SRN thin film was deposited on Au electrodes, b) SRN thin film was deposited on SiO_2 substrate, then Au electrodes were fabricated on top of SRN film; c) image of electrode tips fabricated on SRN film, the electrode gap is 20 µm; d) setup for photocurrent measurement depicting a sample with electrodes (grey) attached, SM fiber patch cable (yellow) with a bare fiber (blue) on the left to couple light onto the sample surface (green arrow), and MM fiber patch cable with a MM bare fiber on the right to couple light out.

mentioning that covers were placed on the top of the samples, specifically in the electrode pads' locations, to protect them from SRN and SiO_2 cladding deposition. This allowed electrode probes to be attached to the corresponding pads, enabling the application of a DC electric field. Notably, the fabrication flow shown in Figure 1a simplified the fabrication process. Indeed, the adopted approach made possible to use the same dose and defocus of the photolithography process, regardless of an SRN thin film refractive index and its thickness, since the film was deposited after the photolithography exposure of an electrode pattern. Note that an optimal dose and defocus would be different for each SRN index if the photolithography was done after SRN thin film deposition. Furthermore, the gap between the electrode tips (electrode gap) was varied in size between 12, 15, and 20 µm to diversify the photocurrent measurement results not to rely on a single measurement per sample. Meanwhile, the electrode length was 50 µm for all samples. The electrode gaps were intentionally made small to enhance the applied DC electric field and, thus, to increase the photocurrent, which was expected to be small in the first place. The thicknesses of electrodes and SRN films were designed to be about 700 nm-thick enough to generate the detectable photocurrent, while avoiding thin film cracking due to stress. Additionally, an alternative fabrication approach, shown in Figure 1b, was implemented to specifically demonstrate the effect of rapid thermal annealing (RTA) on the photocurrent in the fabricated SRN samples (as detailed in Section 2.2). In fact, it was found critical to anneal SRN deposited on a SiO_2 substrate before fabricating the electrodes, since otherwise the electrode tips would bump into each other after annealing, as a consequence of SRN films being compressed during the annealing at high temperatures. In the adopted approach, the photocurrent is still generated in an SRN film even with the presence of SiO_2 between the electrode tips, since the DC electric field permeates the material underneath the electrodes, where there is a contact with an SRN thin film. The electrode gaps and SRN thin film thicknesses for the annealed samples (from Figure 1b) were consistent with those described in Figure 1a, while the thickness of Au electrodes was 400 nm. Finally, Figure 1c shows a microscope image of the electrode tips for the approach presented in Figure 1b.

The setup used to characterize the photocurrent as a function of the SRN index is shown in Figure 1d. A laser (Agilent 81980A), emitting at 1540 nm, was used to illuminate the sample and generate the free carriers. The light was coupled to a single mode (SM) patch cable (mode field diameter ≈10 µm) with a bare fiber tip pointing toward the SRN sample. Since the gap between the fiber tip and the sample surface was on the order of 10 µm, a beam divergence could be neglected since the Rayleigh length was estimated at 50 µm. Therefore, the beam size was maintained at ≈10 µm, as was necessary to fit the SRN aperture located between the electrode tips. At the opposite end of the SRN sample, light was collected by a multi-mode (MM) 50 µm core fiber which facilitated the alignment of the SM fiber relative to the SRN aperture and, thus, maximization of measured photocurrent. A Keithley 2400 source meter was used to apply the DC electric field across the SRN film and measure the generated photocurrent, wherein needle electrodes, connected to the source, were attached to the electrode pads deposited on the SRN samples. The fibers, samples, needle electrodes were placed on positioning stages to allow accurate alignment of all the components.

2.2. Experimental Results

DC voltage of 210 V was applied to the electrode pads to generate and measure the electric current in the SRN samples. Notably, a non-negligible current was observed in the SRN samples even in the absence of laser light. However, a markedly stronger current was detected when the laser was engaged (its power was set to 14 dBm), indicating a presence of strong photocurrent. Under the described conditions it is natural to introduce a total current I, consisting of a sum of the current when there is no light I_0, and the photocurrent I_{ph}, when the sample is exposed to laser light, such that:

$$I = I_0 + I_{ph} \tag{1}$$

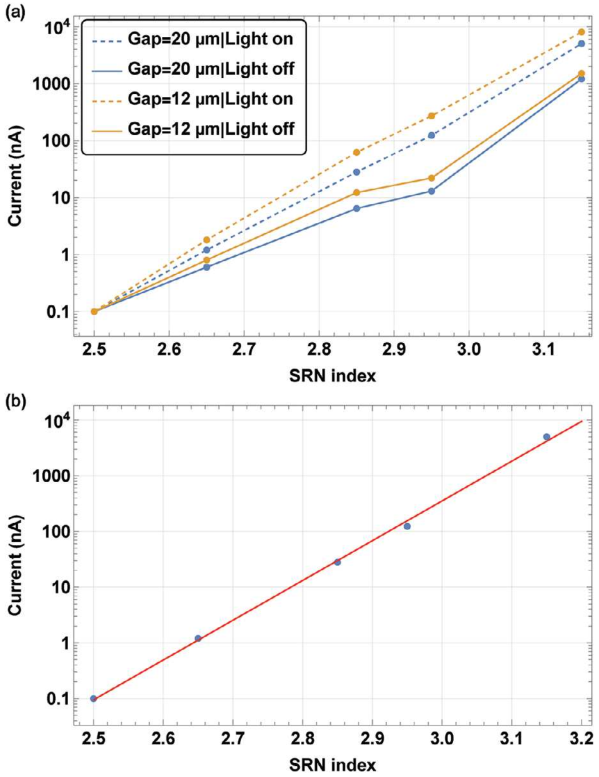

Figure 2. a) Current as a function of an SRN refractive index at 210 V DC. Dashed lines represent the total current I when 14 dBm of power is on (Light on), while solid lines represent the current when there is no light I_0 (Light off), blue is for the electrode gap of 20 μm, orange is for 12 μm; b) total current as a function of an SRN refractive index for the electrode gap of 12 μm (dashed orange line from (a)) fitted by a linear function in Wolfram Mathematica.

Figure 2a shows I and I_0 measured as a function of an SRN refractive index when the DC voltage of 210 V was applied to the electrodes having the gaps of 20 and 12 μm. It is apparent that the current dependence on the SRN index is exponential (i.e., linear in the semi-logarithmic scale) for both electrode gaps, indicating a significant increase in the free carrier concentration in SRN films with a higher index. Note that the experiment was conducted in a dark room to minimize current generation from the ambient light. In particular, Figure 2b demonstrates the total current as a function of an SRN refractive index for the electrode gap of 12 μm fitted by a linear function in Wolfram Mathematica. Based on the fitting, we derived the following formulae for the total current dependence on the SRN refractive index: $I = 10^{-(18.9\pm1.4)+(7.1\pm0.5)n_{srn}}$ for the gap of 20 μm, and $I = 10^{-(19.7\pm1.4)+(7.5\pm0.5)n_{srn}}$ for the gap of 12 μm, where n_{srn} is the SRN refractive index, and the presented error bars are based on 95% confidence intervals. As can be observed in Figure 2a, overall, a stronger current is generated when the electrode gap is smaller due to the consequent larger electric field between the electrodes' tips, as dictated by the Ohm's law. This also demonstrates why it was important to keep the SRN area between the electrodes as small as possible—namely to increase the generated photocurrent so that it can be detected even at lower refractive indices of SRN.

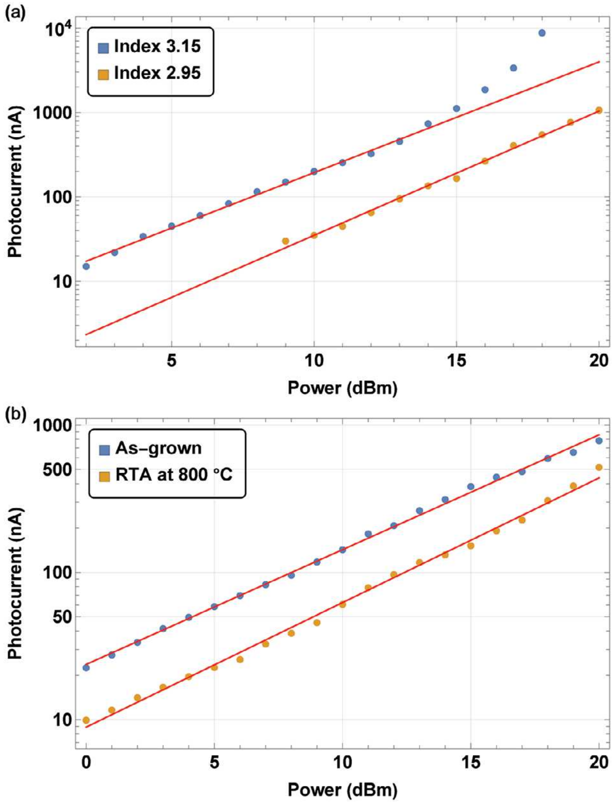

Figure 3. Photocurrent Iph as a function of optical power at 210 V DC applied for a) SRN indices of 3.15 (blue) and 2.95 (orange), b) as-grown SRN film with refractive index of 2.95 (blue) and annealed one at 800 °C (orange). The data was fitted by a linear trend in Wolfram Mathematica.

Notably, both I_0 and I_{ph} appear to be negligible for the lowest SRN index of 2.5. This observation agrees well with the premise that the nonlinear losses observed in SRN waveguides are due to FCA, since the nonlinear losses were not observed in SRN with the index of 2.5, which was demonstrated in our previous work,[1] and will be further elaborated on in the current manuscript in the next section. It suffices to note at this point that the largest photocurrent was observed in the sample with the highest SRN refractive index of 3.15, matching the equivalent result for the nonlinear losses observed in SRN waveguides. Needless to say, the observed behavior strongly implies free carrier generation by the incident light. The generated carriers, in turn, absorb the light, subsequently causing nonlinear losses in SRN waveguides.

We also rigorously measured the photocurrent I_{ph} (defined as $I - I_0$) as a function of optical power in the fabricated SRN samples to determine if it follows a linear trend. The measured curves, fitted by a linear trend in Wolfram Mathematica, are shown in **Figure** 3a for SRN indices of 3.15 and 2.95 with 210 V of DC voltage applied for the 12 μm electrode gap. It can be seen that photocurrent observed in the SRN sample with the index of 3.15 exceeds that measured in the sample with the index of 2.95 for any optical power. Interestingly, it starts growing at a faster rate (at the power of around 15 dBm) than predicted by the linear dependence. The observed rise in photocurrent ultimately leads to electric field breakdown at higher optical power. On the other hand, the SRN sample with the index of 2.95 clearly exhibits a linear dependence of the measured photocurrent, even for higher optical powers. More importantly, no voltage breakdown was observed in the second sample with the refractive index of 2.95, nor has it been observed in any samples with a refractive index lower than 2.95. Overall, the photocurrent is consistently larger for a higher SRN refractive index at any optical power used.

As for the origin of the observed trend, it is well-known that SRN with a higher refractive index contains more Si and hydrogen (H).[1] In fact, the latter is due to the silane SiH_4 gas used in PECVD SRN deposition. Specifically, since the measured photocurrent increases with the SRN sample refractive index, it is crucial to understand whether the increase in Si, H, or both-related defects or impurities are responsible for the observed increase of the photocurrent. Accordingly, with the purpose of determining the effect of Si/H defects or impurities on the photocurrent, we fabricated two identical SRN samples with the index of 2.95 following the approach depicted in Figure 1b, then implemented RTA at 800 °C for 2 min for one sample with the aim of reducing the defect density.[38–40] As a result of the described annealing process, we observed an increase in the sample's refractive index to 3.15, as a consequence of the increased concentration of Si and density of the film. We subsequently measured the photocurrent in the pair of samples (i.e., in an as-grown SRN film and the annealed sample), and it was confirmed that RTA indeed did reduce the photocurrent measured in the corresponding SRN samples with various electrode gaps (12, 15, and 20 µm). The photocurrent was once again captured for this set of samples as a function of optical power. The results are presented in Figure 3b, and, similarly, the photocurrent in the as-grown sample was found to consistently exceed that in the annealed one, despite the fact that the refractive index of the latter was much higher. Therefore, it is straightforward to conclude that RTA at 800 °C for 2 min of SRN results in a reduction of the photocurrent. Since annealing is known to reduce the defect density,[38–40] we hypothesize that the photocurrent is caused by the defects present in SRN samples. On the other hand, the fact that the photocurrent remains relatively large even in the annealed samples implies that either the remaining defects and impurities cause the photocurrent, or there is some other mechanism that may be responsible for carrier generation. In any event, the detailed study of defects and impurities present in SRN, while necessary for full comprehension, is beyond the scope of this manuscript.

3. Nonlinear Loss Dynamics in SRN Waveguides

3.1. Fabrication and Setup

Having established FCA to be the main cause of the nonlinear optical losses in SRN waveguides, we set out to rigorously characterize its dynamics and measure both the associated free carrier generation and recombination lifetimes. For reference, it should be noted that in our previous work,[1] we have determined that TPA is absent in the fabricated SRN waveguides at the power levels where the nonlinear losses are observed. This consideration also indicates that the cause of free carrier generation is related to the defects present in SRN films (as supported by the experimental results in Section 2 above). Therefore, given that larger nonlinear losses were observed in higher refractive indices of SRN waveguides,[1] a reduction of carrier generation and recombination lifetimes is anticipated due to the increase in the defect density. Moreover, it should be possible to avoid nonlinear losses altogether by using optical pulses shorter than the generation lifetime, provided that the pulse repetition period is longer than the recombination lifetime to avoid carrier accumulation and facilitate the carrier recombination process. To strictly determine whether these statements indeed hold true, we assembled the setup presented in **Figure 4a**, which allowed us to characterize the dynamics of the optical pulse transmission in SRN waveguides. In the setup shown in Figure 4a, a 12.5 Gb s^{-1} N4903A pattern generator from Agilent Technologies (generally known as a J-BERT) was used to generate an electrical pulse pattern to drive a 40 GHz lithium niobate intensity modulator, which was used to shape optical pulses by modulating a 1540 nm optical signal emitted by an Agilent 81980A CW laser, after a transverse electric (TE) polarization was set by polarization controllers. A C-band erbium-doped fiber amplifier (EDFA) was used to amplify the optical pulse stream, whereas an optical isolator was placed immediately after the amplifier to prevent the high peak power pulse back reflection into the EDFA. Next, a beam splitter was used to direct –20 dB of the optical pulse power to an HP 83485B 30 GHz optical detector for monitoring on an 83480A digital communications analyzer (DCA) from Hewlett Packard, used as a sampling oscilloscope. The rest of the optical pulse power was coupled to the SRN waveguide under test (the cross-section presented in Figure 4b), after a TE mode was set by polarization controllers. Finally, –10 dB of a transmitted optical pulse was coupled to an optical power meter to measure average transmitted power, while the rest was coupled to an 83440D 32 GHz lightwave detector from Agilent, connected to the sampling oscilloscope to capture and characterize the dynamics of transmitted optical pulses.

The probing (signal) optical pulse (observed on the oscilloscope) had a rise time of about 50 ps and was limited by the rise times of the pattern generator, the sampling oscilloscope, and the 32 GHz photodetector. Consequently, the specified pulse duration allowed reliable measurements of the carrier generation lifetime as short as 50 ps. On the other hand, the maximum repetition pulse period was limited to ≈2 µs, as confirmed experimentally, to ensure that the optical pulse distortion (caused by the EDFA transition dynamics) is avoided. Therefore, the described experimental condition allows the measurement of a carrier recombination lifetime as long as 2 µs. As will be shown later, the observed nonlinear loss dynamics fit well within the specified limits, enabling an accurate determination of both recombination and generation lifetimes. Note that the repetition period shorter than the EDFA transition dynamics, such as in our case, enables enhancement of the peak power Ppeak, with respect to the average power P_{av}, for a pulse duty cycle D, as $P_{peak} = P_{av}/D$. In our case, the pulse duration and repetition period were 200 ns and 2 µs, respectively, leading to a duty cycle of 0.1, and thus, $P_{peak}/P_{av} = 10$, allowing creation of high peak power optical pulses. Therefore, this setup allowed us to increase the peak power without changing the average power by simply altering the pulse duration duty cycle ratio.

In general, it is possible to estimate a free carrier generation lifetime by using only one optical pulse source (signal) by measuring the pulse transmission through a device, even though two sources of light are typically utilized (pulsed pump and CW probe) to measure a recombination lifetime.[34] However, in our

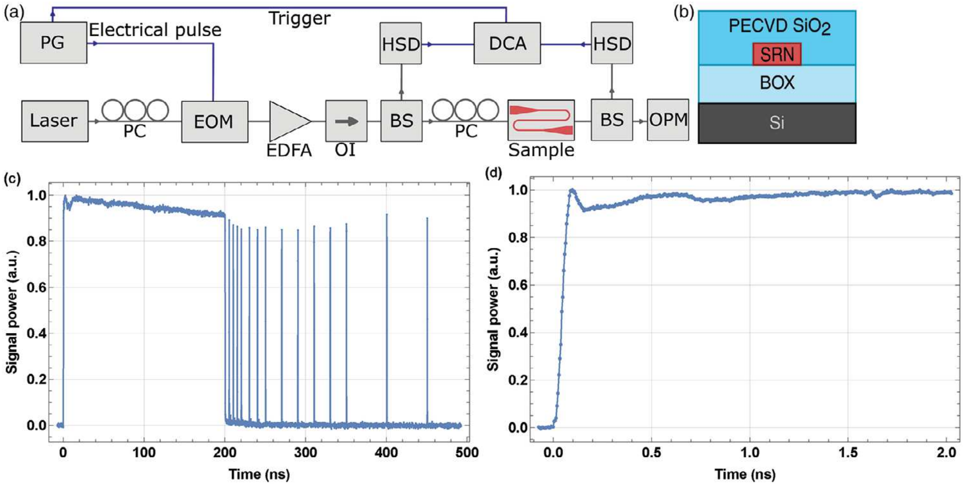

Figure 4. a) Block diagram of the setup used to characterize nonlinear loss dynamics by measuring optical pulse transmission, where blue arrows represent an electrical signal, gray arrows represent an optical signal. PG: Pulse pattern generator as an electrical pulse source, EOM: Electrooptic modulator based on lithium niobate, EDFA: Erbium-doped fiber amplifier, OI: Optical isolator, BS: Beam splitter, PC: Polarization controller, HSD: High speed photodetector, OPM: Optical power meter, DCA: Digital communications analyzers as a sampling oscilloscope. b) Cross-section of an SRN waveguide used in the experiments. Normalized optical power of a signal pulse measured on the oscilloscope, used to characterize the nonlinear loss dynamics in SRN waveguides: c) Large timescale (500 ns) demonstrating a complex shape pulse consisting of a 200 ns pulse followed by a time-comb of short 200 ps pulses, d) short timescale (2.5 ns) demonstrating the front edge of the pulse with the rise time of about 50 ps.

study, we implemented a different approach, taking advantage of the pulse generator's ability to generate non-return-to-zero patterns (a binary code). Specifically, a generated waveform used to probe the SRN samples consisted of two parts, where the first part was a continuous 200 ns long optical pulse that generated free carries, while the second part consisted of a series of short isolated 200 ps pulses, in effect forming a comb in the time domain, as demonstrated in Figure 4c. Such a comb created only a negligible concentration of free carriers, since the duration of each constituent pulse was shorter than the free carrier generation lifetime, thus not affecting the free carrier recombination. Therefore, the lifetime of the latter can be estimated simply by observing the response dynamics of the comb at the output of the SRN waveguide under test (i.e., transmission dynamics). Consequently, as explained above, our novel approach allowed us to characterize both generation and recombination lifetimes based on transmission dynamics, by using just an optical pulse signal, simplifying the free carrier dynamics characterization. Additionally, Figure 4d shows the front edge of the 200 ns optical pulse (same as from Figure 4c) exiting from the EDFA, and it can be seen that the rise time is around 50 ps. The minor amplitude variation (<10%), that is observed in both Figure 4c,d, is caused by the transient dynamics of EDFA.

To demonstrate how FCA dynamics changes with the SRN index, multiple SRN waveguides with the length of 6.5 mm were fabricated for the indices of 2.5, 2.7, 3.0, and 3.15, and the corresponding widths of the waveguides were 550, 500, 440, and 375 nm, while the corresponding thicknesses were 383, 386, 337, and 343 nm, similar to these used in our previous work.[1] Fully etched linearly apodized grating couplers (GC) were used to couple light in and out of waveguides, while 300 μm long tapers were used to adiabatically change the mode size.[41] Specifically, the following fabrication flow was utilized[1]: First, Si device layer was removed from silicon on insulator (SOI) substrates by a tetramethylammonium hydroxide (TMAH) wet etching such that only 3 μm of the buried oxide (BOX) was left on the top of the Si substrate (note that this step can be avoided if Si samples with only SiO$_2$ layer on the top are available). Then, a PECVD SRN thin film was deposited in an Oxford Plasmalab PECVD system, where the SiH$_4$ with N$_2$ precursor gases were used, with the chamber temperature set to 350 °C, and pressure to 650 mTorr (the same as in section 2). Next, e-beam lithography was implemented to expose an hydrogen silsesquioxane (HSQ) e-beam resist spun on SRN thin films. After HSQ development, the sample was etched in an Oxford Plasmalab P100 system, and HSQ was removed by 6:1 buffered oxide etch (BOE) solution mixed with de-ionized (DI) water in the ratio of 1:10. Finally, the samples were clad with 1 μm of a PECVD SiO$_2$ deposited by the Oxford Plasmalab PECVD system. The cross-section of the device is demonstrated in Figure 4b.

Table 1 summarizes some important parameters of our fabricated samples,[1] including the SRN refractive index n_{srn}, the waveguide core width w, the waveguide core thickness d, the overlap integral estimated from Lumerical (Ansys) simulations Γ, the linear optical loss coefficient α measured by a cut-back method, the GC coupling efficiency per one grating μ. It is worth noting that due to a change of an SRN refractive index it was necessary

Table 1. SRN waveguide and GC parameters for different samples used in the experiments.

n_{srn}	w [nm]	d [nm]	Γ	α [dB cm^{-1}]	μ [dB]
2.5	550	383	0.49	8	−6.8
2.7	500	386	0.51	16	−4.4
3	440	337	0.5	19	−4.9
3.15	375	343	0.42	21	−6

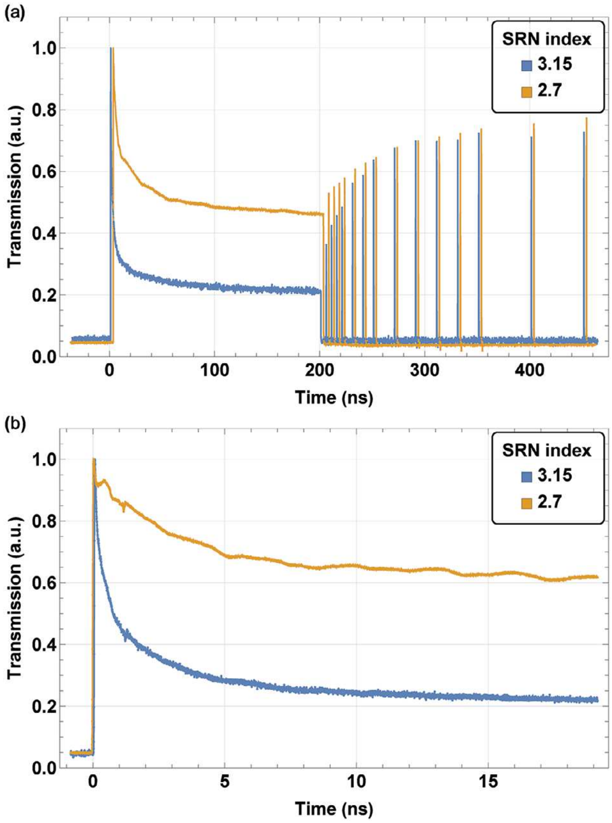

Figure 5. Optical pulse transmission dynamics in an SRN waveguide measured on the oscilloscope at the coupled peak power of around 21 dBm for the indices of 3.15 (blue) and 2.7 (orange), a) Large timescale (500 ns) demonstrating a 200 ns pulse followed by a comb of short pulses, b) short timescale (20 ns) demonstrating the front edge of the pulse affected by the nonlinear loss dynamics.

to adjust the geometry of a waveguide to maintain a consistent mode overlap integral. At the same time, changing the geometry of the waveguides may affect surface recombination, altering a free carrier lifetime. Therefore, the waveguide geometries of the samples were kept as similar as possible to minimize the effect on measurements when comparing data from samples with different indices.

3.2. Experimental Results

Figure 5a demonstrates the dynamics of the transmitted optical pulses for the peak power of 21 dBm coupled to SRN waveguides. As evident in Figure 5a, a sharp drop in transmitted power by about 80% and 50% is observed for sample indices of 3.15 and 2.7, respectively, indicating a strong nonlinear loss effect. Furthermore, the time-comb structure, following the long pulse, effectively sampled the recombination process with the comb pulses' amplitudes growing in time. Lastly, the carrier generation dynamics, captured by the long (200 ns) pulse from Figure 5a, is presented on a shorter timescale in Figure 5b to demonstrate explicitly that most of the power transmission decline happens on the scale of 10 ns.

It is also worth noting that while the signal pulse distortion can be observed in Figure 4d, it is deemed insignificant since its maximum amplitude variation is less than 10%, i.e., negligible compared to the amplitude decline caused by the nonlinear losses (i.e., 50–80% from Figure 5a). In a similar fashion, the EDFA-caused long pulse drop observed in Figure 4c does not contribute to the captured dynamics significantly. Indeed, the total amplitude change is about 10% over 200 ns time-window of the pulse duration. However, within the scale of 10 ns where the nonlinear loss dynamics primarily occurs, the EDFA-caused amplitude change is only around 0.5%, which can be neglected with respect to the magnitude of the nonlinear losses. Therefore, based on the presented arguments, the generated optical pulse signal can indeed be used to accurately characterize transmission dynamics, thus enabling estimation of generation and recombination lifetimes with relatively high accuracy. Interestingly, we can see that the nonlinear loss dynamics presented in Figure 5b is much smoother for the SRN refractive index of 3.15 since it is mostly affected by the faster carrier generation dynamics, as evident by the sharper decline of the pulse transmission. Meanwhile, in the case of index 2.7, the carrier dynamics is clearly slower and is slightly affected by the signal pulse perturbations seen in Figure 4d. This example also demonstrates why it was important to use longer waveguides and higher optical signal power, thus causing stronger nonlinear losses—namely to increase the accuracy of the measurements by minimizing the impact of the generated signal pulse deviation from an ideal boxcar function.

In principle, we can introduce the signal loss a (i.e., a reduction in transmission caused by the nonlinear loss) such that $a = 1 - T$, where T is the normalized signal transmission of the optical pulse signal, as shown, for example, in Figure 5a. Then, the free carrier generation and recombination lifetimes can be extracted from the captured transmission T or signal loss a dynamics assuming the underlying first order model:

$$\frac{\mathrm{d}T_i}{\mathrm{d}t} = \Delta T_i - \frac{T_i}{\tau_i} \tag{2}$$

$$\frac{\mathrm{d}a_i}{\mathrm{d}t} = \Delta a_i - \frac{a_i}{\tau_i} \tag{3}$$

where the indices $i = g$ or $i = rec$ refer to the generation or recombination dynamics, respectively, t is time, ΔT (or Δa) is the signal transmission (or loss) change rate, and τ is the carrier generation/recombination lifetime. Note that Equations (2) and (3), which are identical to that describing the free carrier concentration dynamics, have a straightforward solution:

$$T_i(t) = \Delta T_i \tau_i (1 - e^{-t/\tau_i}) \tag{4}$$

$$a_i(t) = \Delta a_i \tau_i (1 - e^{-t/\tau_i}) \tag{5}$$

It is worth noting that when considering carrier generation dynamics, it is more convenient to work with the signal loss dynamics which follows Equation (5), since in this case Δa_g acquires a physical meaning of a normalized signal loss rate (measured in s^{-1}), which is proportional to the free carrier concentration generation rate. At the same, the value τ_g is defined as the time it takes for the signal loss to reach the $a_{max}(1 - 1/e)$ level,

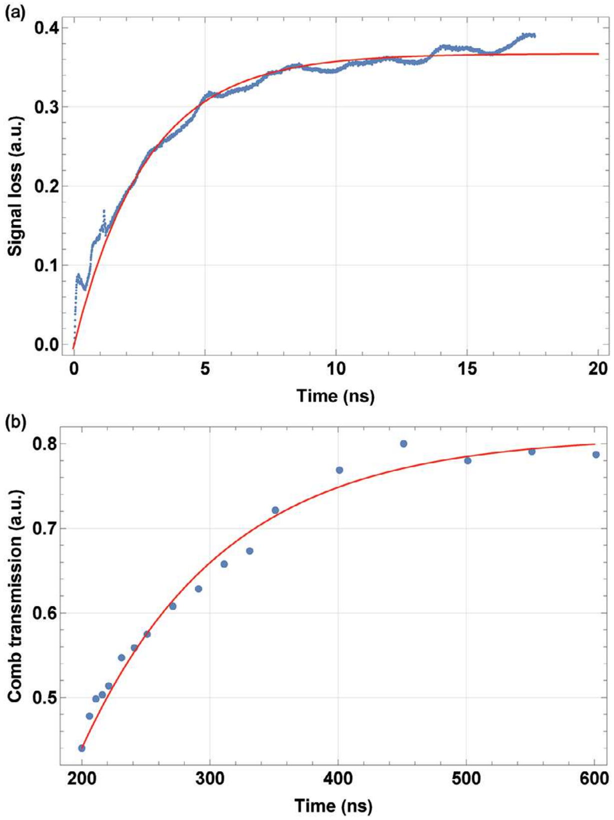

Figure 6. a) Dynamics of signal loss a in an SRN waveguide caused by free carrier generation at the coupled peak power of around 21 dBm for the index of 2.7, fitted using Equation (5) in Wolfram Mathematica, b) transmission dynamics of the comb in an SRN waveguide demonstrating free carrier recombination dynamics at the coupled peak power of around 21 dBm for the index of 2.7, where dots represent the transmission peaks of each pulse in the comb, fitted using Equation (4) in Wolfram Mathematica.

where $a_{max} = \Delta a_g \tau_g$ is the maximum signal loss achieved in the limit $t \gg \tau_g$, as follows from Equation (5), and denotes the free carrier generation lifetime. Hence, the important parameters such as Δa_g and τ_g can be retrieved from fitting the signal loss dynamics, as shown in **Figure 6**a. Likewise, Equation (4) allows estimation of the recombination lifetime τ_{rec}, although in our case the transmission dynamics of the time-comb is used for the parameter extraction instead. With that purpose, we measured the transmission peaks of each pulse from the time-comb and fitted them to the function described by Equation (4), as shown in Figure 6b, to retrieve the recombination lifetime τ_{rec}.

Figure 7a shows the signal loss rate Δa_g as a function of the pulse peak power (coupled to the waveguide) for various SRN indices extracted from the captured carrier dynamics. As can be seen in Figure 7a, the signal loss rate increases with both the peak power and the SRN index. Specifically, the increase of signal loss rate Δa_g with power is recognized as linear, implying that the free carrier concentration is proportional to the incident optical power, as expected. Indeed, the linear relation suggests that the free carriers are not generated by TPA (which would lead to a quadratic dependence of free carrier concentration on power), but rather by defects in SRN. Likewise, Figure 7b shows free carrier generation lifetime τ_g as a function of the peak power and the SRN index, and we can observe that τ_g reduces with both parameters. Furthermore, the evolution of Δa_g and τ_g is necessarily correlated since the larger Δa_g depletes the propagating pulse at a faster rate, resulting in a reduction of τ_g. However, it is also reasonable to separate these quantities since they have a distinct physical meaning, as explained in the paragraph above. Overall, the shortest generation lifetime measured in our experiments is around 500 ps, and it was captured for the highest peak power of 24 dBm (coupled to the waveguide) for the sample with the refractive index of 3.15. More importantly, the last quoted value for the carrier lifetime is important since it strictly determines how short the pulses need to be in order to minimize (or avoid) the FCA dynamics and, therefore, the undesired nonlinear losses. Consequently, it can be concluded that for the index of 3.15, the nonlinear losses significantly decrease for pulses shorter than 500 ps. Similarly, for the index of 2.7 and the peak power of 25 dBm, the pulse duration should be less than 2 ns to minimize the effects of FCA. Thus, a reduction in the SRN refractive index provides a dual advantage: it leads to a decrease in the magnitude of the nonlinear losses determined by Δa_g, and it also increases the maximum pulse duration that can be used without experiencing the nonlinear losses. However, as demonstrated in detail in ref. [1], this trend, unfortunately, also leads to a steady reduction in the SRN optical nonlinear response, indicating a tradeoff between the nonlinearities and losses. For completeness, we also note that no nonlinear losses were observed for the SRN samples with the index of 2.5 (and, thus, the results are not presented here).

Lastly, Equation (5) implies that the signal loss (or transmission) eventually reaches a steady state (i.e., saturation) at the value of $a_{max} = \Delta a_g \tau_g$, which can be observed when the incident pulse duration is much longer than the free carrier generation lifetime τ_g. For reference, the latter case is observed in Figure 5a for the 200 ns pulse. In other words, the saturation implies that the steady state is achieved in the carrier generation dynamics, with no further growth in the free carrier concentration. Therefore, the minimum transmission $1 - a_{max}$ at the saturation is an important parameter that describes the maximum nonlinear losses achieved in a steady state in both pulsed and CW excitation regimes. Hence, the minimum transmission was estimated from the measured free carrier generation dynamics, shown in Figure 5a, as a function of the peak pulse power and presented in **Figure 8**a. Evidently, we observed the minimum transmission of about –8 dB for the highest SRN index of 3.15 at the peak power of 24 dBm. The minimum steady-state transmission increases to the value of about –2 dB as the peak power is reduced to 12 dBm. Finally, we also point out that it is possible to reduce the transmission losses to just 1–3 dB by utilizing SRN waveguides with the index of 2.7 at the peak powers in the range of 14–25 dBm. Overall, the results align with the conclusions drawn in the preceding paragraph, indicating that a reduction in the SRN index correlates with a decrease in Δa_g.

Figure 8b demonstrates the recombination lifetimes τ_{rec} obtained from the fitting presented in Figure 6b for a set of varying refractive indices and pulse peak powers (coupled to the SRN waveguide). Remarkably, like in the case of the free carrier generation lifetime τ_g, increasing the refractive index of SRN leads to larger recombination lifetimes, which may indicate higher concentration of defects participating in the recombination.

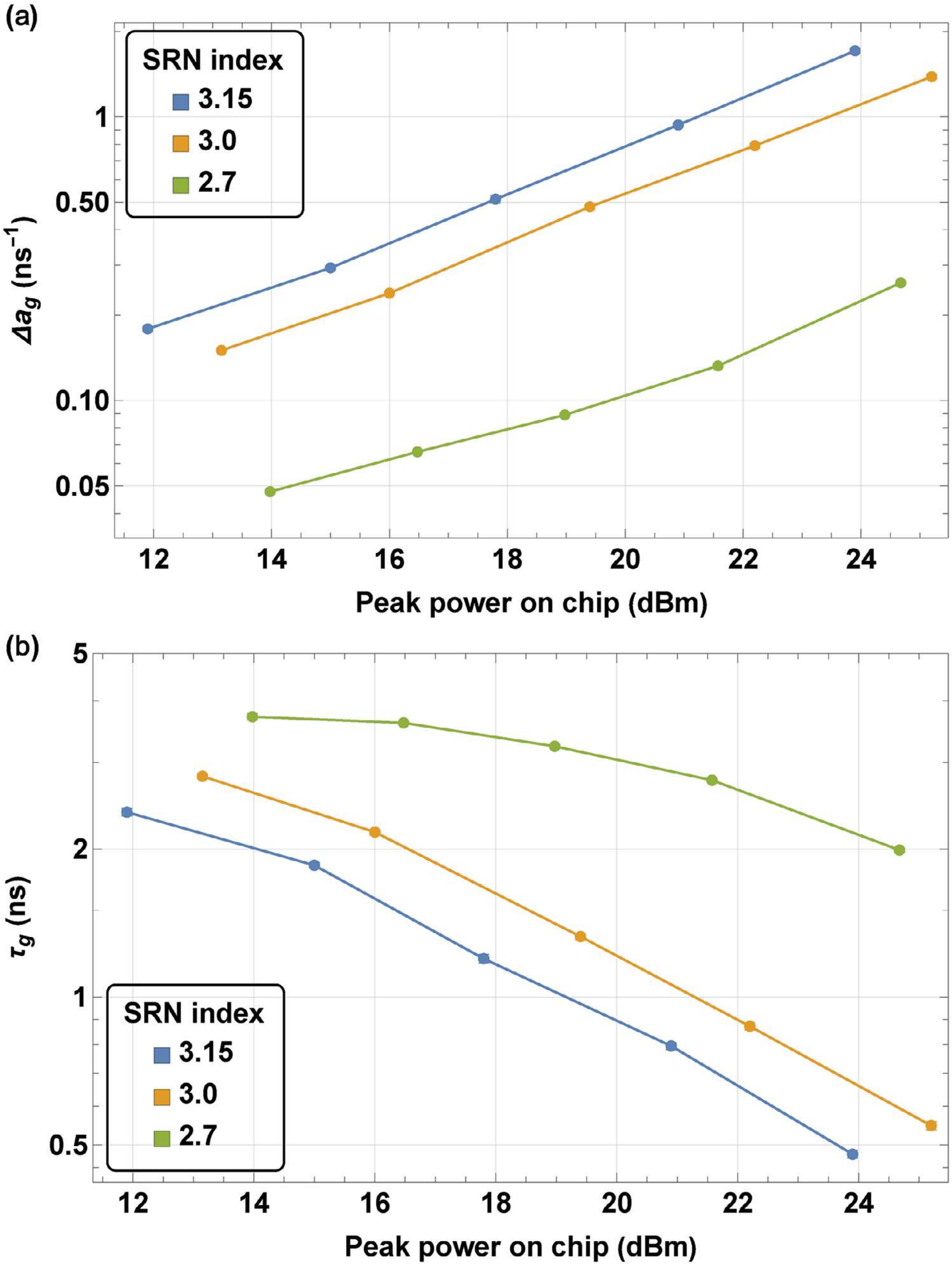

Figure 7. a) Signal loss rate Δa_g as a function of a pulse peak power coupled to an SRN waveguide for the indices of 3.15 (blue), 3 (orange), 2.7 (green), b) carrier generation lifetime τ_g as the function of pulse power coupled to an SRN waveguide for the indices of 3.15 (blue), 3 (orange), 2.7 (green). The error bars are obtained from fitting in Wolfram Mathematica and are based on 95% confidence intervals (they are small and obscured by the data points).

However, it is also important to note that the recombination lifetimes do not change with the peak power within the margins of errors, contrary to the case of carrier generation lifetimes, which indicates an absence of Auger recombination mechanism.[28] Overall, the largest recombination lifetime, which was measured in an SRN waveguide with the index of 2.7, is around (92 ± 7) ns (averaged over 5 points representing different peak powers, where a margin of error represents a standard deviation error), while it is (39 ± 3) ns and (31 ± 2) ns for the indices of 3 and 3.15, respectively. We also note that the recombination lifetimes play an important role in optical pulse tailoring with the purpose of avoiding nonlinear losses. Indeed, as stated previously (and repeated here for completeness) the pulse repetition time ought to be longer than the sample recombination lifetime to allow the free carriers to recombine, prior to the arrival of the next pulse.

Having determined the free carrier generation and recombination lifetimes, it was possible to optimize optical pulse's duration

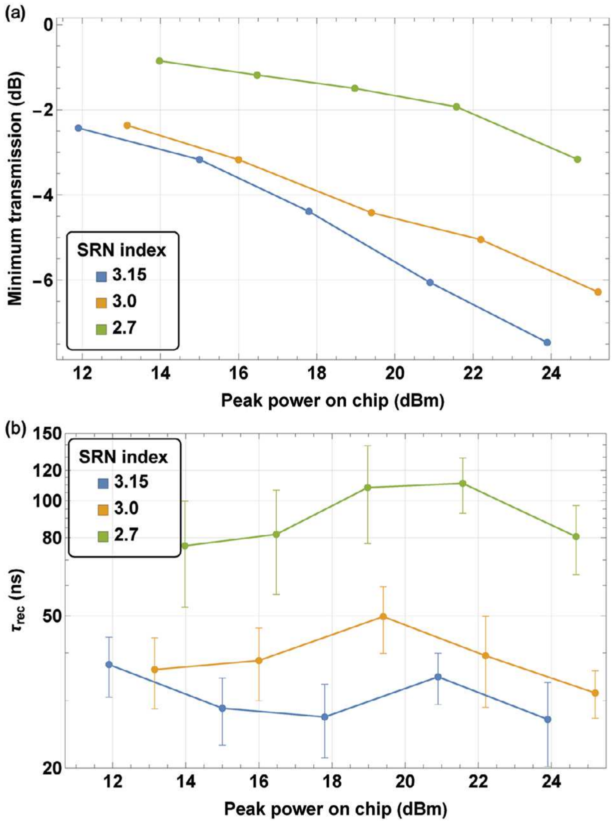

Figure 8. a) Minimum transmission of the pulse as the function of pulse power coupled to an SRN waveguide for the indices of 3.15 (blue), 3 (orange), 2.7 (green), b) recombination lifetime τ_{rec} as function of a pulse peak power coupled to an SRN waveguide for the indices of 3.15 (blue), 3 (orange), 2.7 (green).

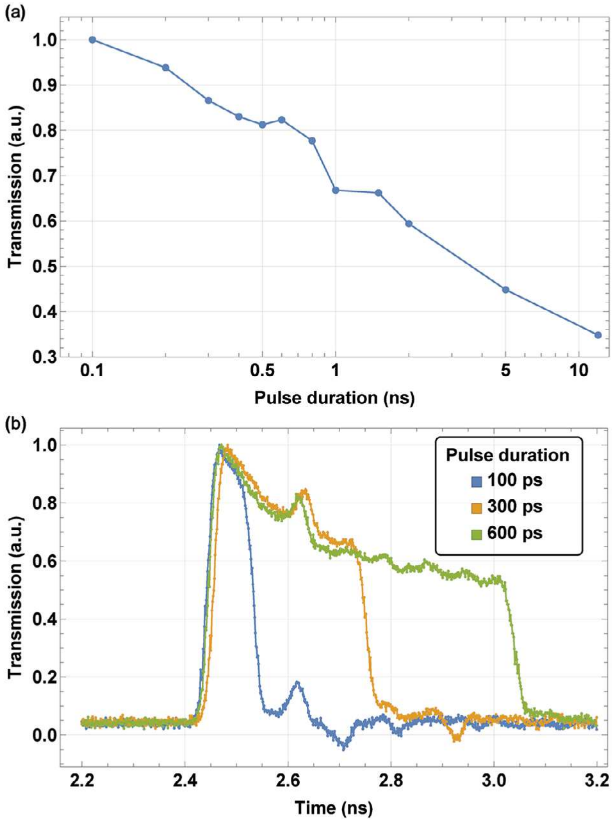

Figure 9. a) Pulse transmission as a function of the pulse duration for SRN index of 3.15 and coupled peak power of 24 dBm, b) pulse transmission dynamics for the pulse durations of 100 ps (blue), 300 ps (orange), 600 ps (green) for SRN index of 3.15 and coupled peak power of 24 dBm.

and repetition rate to minimize nonlinear optical losses. Indeed, one should expect that if the pulse duration is set to be shorter than τ_g, and the repetition period longer than τ_{rec}, free carriers dynamics will be unable to affect propagating optical pulses, as discussed above. In fact, with that purpose we measured the transmission of an optical pulse (with the repetition period of 2 μs, larger than τ_{rec}) in an SRN waveguide, with the index of 3.15 at the coupled peak power of 24 dBm, as a function of the pulse duration and presented the result in **Figure 9**a. Note that the transmission was calculated as an energy of the transmitted pulse divided by the energy of the signal pulse coming from the EDFA, after which it was normalized by the maximum value (measured at 100 ps pulse duration). As expected, a sharp increase in the transmission is observed as the pulse gets shorter. For completeness, Figure 9b shows transmission of optical pulses for different pulse durations. As clearly demonstrated by the results in Figure 9b, the part of the pulse, characterized by the sharp decline of amplitude (due to the FCA), can indeed be significantly shortened by decreasing the pulse duration, thus leaving only the part of the pulse least affected by the FCA. Hence, it enables utilization of high index SRN waveguides for certain applications where short optical pulses can be used, while avoiding the nonlinear losses and benefiting from the large optical nonlinearities of SRN.[1]

4. Discussion

In summary, we have provided compelling and detailed evidence that the observed nonlinear optical losses in SRN waveguides are attributed to FCA. Indeed, we observed photocurrent in SRN thin films with the refractive indices in the range of 2.65–3.15, which serves as a clear signature of the generated free carriers, and determined that it increases with the SRN refractive index. Similarly, we established that the nonlinear optical losses observed in SRN waveguides, within a comparable range of the refractive indices, also increase with the refractive index. On the other hand, negligible photocurrent in the SRN thin films and absence of nonlinear losses in the corresponding waveguides were observed for the index of 2.5, clearly indicating the absence of free carriers in this case. The aforementioned set of circumstances strongly supports the hypothesis that the photocurrent and the nonlinear losses indeed have the same origin—namely the generated free carriers. Furthermore, it is evident that the free carriers are not generated by TPA, since the last was not observed at the optical powers used in this work.[1] Additionally, it was found that the signal loss rate Δa_g, which is proportional to the free carrier generation rate, grows linearly with the optical pulse peak power, as in the case when defects generate free carriers. We, therefore, conclude that various defects and/or impurities present in SRN films with a large refractive index facilitate both the free carrier generation and recombination processes. Moreover, based on the FCA dynamics observed in SRN waveguides, we determined that both free carrier generation and recombination lifetimes decrease with the refractive index of SRN samples, stemming from the associated increase of the defect density in SRN samples with higher refractive indices. Specifically, the free carrier recombination lifetimes of (92 ± 7) ns, (39 ± 3) ns, and (31 ± 2) ns were estimated for the SRN indices of 2.7, 3, and 3.15, respectively. Notably, voltage breakdown was observed in an SRN thin film for the highest index of 3.15 at a relatively low DC electric field of around 20 $\mathrm{V\,\mu m^{-1}}$, and it can be explained by the presence of a high defect density in the SRN film.[42–44] On the other hand, a noticeable reduction of the photocurrent was observed in the SRN thin film after RTA at 800 °C for 2 min, compared to the as-grown SRN thin film under the same conditions. We, therefore, hypothesize that it indicates the increased incorporation of defects and impurities in as-grown SRN films, owing to the prior ample evidence that RTA reduces defect density.[30–32] Nonetheless, it ought to be stated that while the origin of the observed nonlinear losses is FCA caused by the defects, the origin of the defects has not been established directly, indicating that further research is needed. Finally, and perhaps most importantly, we have demonstrated that it is possible to reduce or avoid nonlinear optical losses in SRN waveguides altogether by utilizing optical pulses shorter than the free carrier generation lifetime while maintaining a repetition period of the pulses longer than the free carrier recombination lifetime. Consequently, the presented results strictly delineate the conditions for taking full advantage of the large nonlinearities in high index SRN ($\chi_3 = (12.6 \pm 1.4) \times 10^{-19}\ \mathrm{m^2\,V^{-2}}$ corresponding to the SRN index of 3.2[1]), leading to its efficient application in nonlinear optics. In the future, we plan to investigate other methods to reduce nonlinear losses, determine the origin of defects responsible for free carrier generation and recombination, and research the spectral response of nonlinear losses to further enhance our understanding of the SRN platform.

Acknowledgements

The authors thank SDNI and all UCSD's nano3 cleanroom staff and Dr Maribel Montero for their assistance with samples fabrication. This work was supported by the Defense Advanced Research Projects Agency (DARPA) DSO's NAC and NLM Programs, the National Science Foundation (NSF) grants NSF ECCS-2023730 and NSF ECCS-2217453, the Army Research Office (ARO), the San Diego Nanotechnology Infrastructure (SDNI) supported by the NSF National Nanotechnology Coordinated Infrastructure (grant ECCS-2025752), and the ASML/Cymer Corporation.

Conflict of Interest

The authors declare no conflict of interest.

Author Contributions

All authors have accepted responsibility for the entire content of this manuscript and approved its submission.

Data Availability Statement

The datasets generated during and/or analyzed during the current study are available from the corresponding author on reasonable request.

Keywords

free carrier absorption, integrated photonics, nonlinear optical losses, photo-induced current, silicon nitride

Received: May 12, 2024
Revised: September 25, 2024

---

[1] D. Belogolovskii, N. Alic, A. Grieco, Y. Fainman, *Adv. Photonics Res.* **2024**, 2400017.
[2] K. J. A. Ooi, D. K. T. Ng, T. Wang, A. K. L. Chee, S. K. Ng, Q. Wang, L. K. Ang, A. M. Agarwal, L. C. Kimerling, D. T. H. Tan, *Nat. Commun.* **2017**, *8*, 13878.
[3] D. T. H. Tan, K. J. A. Ooi, D. K. T. Ng, *Photon. Res.* **2018**, *6*, B50.
[4] J. W. Choi, G. F. R. Chen, D. K. T. Ng, K. J. A. Ooi, D. T. H. Tan, *Sci. Rep.* **2016**, *6*, 27120.
[5] Y. Cao, B.-U. Sohn, H. Gao, P. Xing, G. F. R. Chen, D. K. T. Ng, D. T. H. Tan, *Sci. Rep.* **2022**, *12*, 9487.
[6] T. Wang, D. K. T. Ng, S.-K. Ng, Y.-T. Toh, A. K. L. Chee, G. F. R. Chen, Q. Wang, D. T. H. Tan, *Laser Photonics Rev.* **2015**, *9*, 498.
[7] A. Friedman, H. Nejadriahi, R. Sharma, Y. Fainman, *Opt. Lett.* **2021**, *46*, 4236.
[8] G.-R. Lin, S.-P. Su, C.-L. Wu, Y.-H. Lin, B.-J. Huang, H.-Y. Wang, C.-T. Tsai, C.-I. Wu, Y.-C. Chi, *Sci. Rep.* **2015**, *5*, 9611.
[9] C. Lacava, T. D. Bucio, A. Z. Khokhar, P. Horak, Y. Jung, F. Y. Gardes, D. J. Richardson, P. Petropoulos, F. Parmigiani, *Photon. Res.* **2019**, *7*, 615.
[10] H.-H. Lin, R. Sharma, A. Friedman, B. Cromey, F. Vallini, M. Puckett, K. Kieu, Y. Fainman, *APL Photonics* **2019**, *4*, 036101.
[11] E. Timurdogan, C. V. Poulton, M. J. Byrd, M. R. Watts, *Nat. Photonics* **2017**, *11*, 200.
[12] J. Peltier, W. Zhang, L. Virot, C. Lafforgue, L. Deniel, D. Marris-Morini, G. Aubin, F. Amar, D. Tran, X. Yan, C. G. Littlejohns, C. Alonso-Ramos, K. Li, D. J. Thomson, G. Reed, L. Vivien, *Photon. Res.* **2024**, *12*, 51.
[13] B. Zabelich, C. Lafforgue, E. Nitiss, A. Stroganov, C.-S. Brès, *APL Photonics* **2024**, *9*, 016101.
[14] H. Nejadriahi, A. Friedman, R. Sharma, S. Pappert, Y. Fainman, P. Yu, *Opt. Express* **2020**, *28*, 24951.
[15] A. Friedman, D. Belogolovskii, A. Grieco, Y. Fainman, *Opt. Express* **2022**, *30*, 45340.
[16] H. Nejadriahi, S. Pappert, Y. Fainman, P. Yu, *Opt. Lett.* **2021**, *46*, 4646.
[17] H. Nejadriahi, P. Gaur, K. Johnson, S. Pappert, Y. Fainman, P. Yu, *Opt. Lett.* **2023**, *48*, 807.
[18] C. Lacava, S. Stankovic, A. Z. Khokhar, T. D. Bucio, F. Y. Gardes, G. T. Reed, D. J. Richardson, P. Petropoulos, *Sci. Rep.* **2017**, *7*, 22.
[19] B.-U. Sohn, J. W. Choi, D. K. T. Ng, D. T. H. Tan, *Sci. Rep.* **2019**, *9*, 10364.
[20] N. Wright, D. Thomson, K. Litvinenko, W. Headley, A. Smith, A. Knights, J. Deane, F. Gardes, G. Mashanovich, R. Gwilliam, G. Reed, *Opt. Express* **2008**, *16*, 19779.
[21] C.-W. Chen, L. V. Nguyen, K. Wisal, S. Wei, S. C. Warren-Smith, O. Henderson-Sapir, E. P. Schartner, P. Ahmadi, H. Ebendorff-Heidepriem, A. D. Stone, D. J. Ottaway, H. Cao, *Nat. Commun.* **2023**, *14*, 7343.
[22] C. Wolff, M. J. A. Smith, B. Stiller, C. G. Poulton, *J. Opt. Soc. Am. B* **2021**, *38*, 1243.
[23] R. Claps, D. Dimitropoulos, V. Raghunathan, Y. Han, B. Jalali, *Opt. Express* **2003**, *11*, 1731.
[24] O. Boyraz, T. Indukuri, B. Jalali, *Opt. Express* **2004**, *12*, 829.
[25] L. Yin, G. P. Agrawal, *Opt. Lett.* **2007**, *32*, 2031.
[26] M. Rumi, J. W. Perry, *Adv. Opt. Photon.* **2010**, *2*, 451.

[27] Y. Zhang, C. Husko, S. Lefrancois, I. H. Rey, T. F. Krauss, J. Schröder, B. J. Eggleton, *Opt. Express* **2016**, *24*, 443.
[28] R. F. Pierret, *Advanced Semiconductor Fundamentals*, Prentice Hall, Upper Saddle River, NJ **2003**.
[29] D. Schroder, *IEEE Trans. Electron Devices* **1997**, *44*, 160.
[30] A. Blanco-Redondo, D. Eades, J. Li, S. Lefrancois, T. F. Krauss, B. J. Eggleton, C. Husko, *Optica* **2014**, *1*, 299.
[31] W. He, A. Zakar, T. Roger, I. V. Yurkevich, A. Kaplan, *Opt. Lett.* **2015**, *40*, 3889.
[32] D. E. Hagan, M. Nedeljkovic, W. Cao, D. J. Thomson, G. Z. Mashanovich, A. P. Knights, *Opt. Express* **2019**, *27*, 166.
[33] D. Navarro-Urrios, A. Pitanti, N. Daldosso, F. Gourbilleau, R. Rizk, G. Pucker, L. Pavesi, *Appl. Phys. Lett.* **2008**, *92*, 051101.
[34] M. Novarese, S. Romero-Garcia, J. Bovington, M. Gioannini, *IEEE Photonics Technol. Lett.* **2023**, *35*, 450.
[35] B. Davidson, G. Lucovsky, G. Parsons, R. Nemanich, A. Esser, K. Seibert, H. Kurz, *J. Non-Cryst. Solids* **1989**, *114*, 579.
[36] A. C. Turner-Foster, M. A. Foster, J. S. Levy, C. B. Poitras, R. Salem, A. L. Gaeta, M. Lipson, *Opt. Express* **2010**, *18*, 3582.
[37] A. Gil-Molina, I. Aldaya, J. L. Pita, L. H. Gabrielli, H. L. Fragnito, P. Dainese, *Appl. Phys. Lett.* **2018**, *112*, 251104.
[38] H. Kim, J. Aziz, V. D. Chavan, D. kee Kim, *Curr. Appl. Phys.* **2024**, *57*, 59.
[39] K. Andersen, W. Svendsen, T. Stimpel-Lindner, T. Sulima, H. Baumgártner, *Appl. Surf. Sci.* **2005**, *243*, 401.
[40] E. S. Andrés, A. del Prado, F. L. Martínez, I. Mártil, D. Bravo, F. J. López, *J. Appl. Phys.* **2000**, *87*, 1187.
[41] R. Marchetti, C. Lacava, A. Khokhar, X. Chen, I. Cristiani, D. J. Richardson, G. T. Reed, P. Petropoulos, P. Minzioni, *Sci. Rep.* **2017**, *7*, 16670.
[42] S. Habermehl, R. T. Apodaca, R. J. Kaplar, *Appl. Phys. Lett.* **2009**, *94*, 012905.
[43] C. Ying, T. Ma, L. Xu, M. Rahmani, *Nanomaterials* **2022**, *12*, 14.
[44] W. S. Lau, S. J. Fonash, J. Kanicki, *J. Appl. Phys.* **1989**, *66*, 2765.